Cambridge Centre for Computational Chemical Engineering

University of Cambridge

Department of Chemical Engineering

Simulating the Structural Evolution of Droplets Following Shell Formation

Christopher Handscomb [1]   Markus Kraft [1]

released: 22 December 2008

[1] Department of Chemical Engineering
University of Cambridge
Pembroke Street
Cambridge CB2 3RA
UK
E-mail: mk306@cam.ac.uk

c4e

Abstract

Building on the new droplet drying framework developed by Handscomb et al. [22, 23], this paper develops physically motivated criteria for dynamically deciding the appropriate structural sub-model to use at each stage of the drying process. Such criteria create a spatially resolved mechanistic droplet drying model which, for the first time, is capable of simulating multiple dried-particle morphologies based on evolving droplet composition and drying conditions. The new criteria are used in conjunction with the previously described model framework to simulate colloidal silica droplets, investigating the relationship between suspended particle size and dried-particle morphology.

Contents

1 Introduction

Products as diverse as high value pharmaceuticals and bulk commodities such as dried milk and detergent powders are produced by spray drying [34]. The needs of these differing applications vary greatly. When producing pharmaceuticals it is essential to maintain a sterile environment, whilst food products must be dried in a way that ensures aromas and nutrients are retained. Detergent powders require tightly controlled physical properties if customer demands concerning flowability and dissolution rate are to be met and, for any bulk drying operation, energy efficiency is likely to be a principle concern [12]. The spray drying operation may be tailored to suit all of these roles and many more.

Spray drying works by contacting an atomised feed with drying air in a chamber. The removal of moisture from a spray of droplets involves simultaneous heat and mass transfer and, uniquely in a spray dryer, this process is coupled to concurrent particle formation. When drying droplets containing dissolved or suspended solids, a wealth of different dried-particle morphologies may form. Which type of particle forms depends upon the composition, size, temperature and drying history of the droplet, [40]. Further, because droplet drying and particle formation occur simultaneously, the drying mechanism and resultant kinetics are, in turn, strongly dependent on the evolving droplet microstructure, [27]. Simulating the structural evolution of single droplets within a spray tower continues to present substantial challenges to the modeller, [32].

Handscomb et al. [22] presented a new model for simulating the drying of slurry droplets consisting of an ideal binary solution containing suspended solids. These solids were handled using a population balance approach, enabling the modelling of particle nucleation and growth from the solution. This core model was then extended by Handscomb et al. [23], incorporating a number of sub-models to allow simulation of morphological evolution following formation of a surface shell. The **aims of this paper** are to provide physical motivation for these sub-models and thereby develop logical criteria for deciding when each model should be applied. Such criteria allow simulation of structural evolution as influenced by changing droplet composition and external drying conditions. This is demonstrated by a parameter study investigating the influence of suspended particle size on dried-particle morphology when drying droplets of colloidal silica.

2 Review of Droplet Drying Behaviour and Modelling Approaches

Droplet drying and particle formation occur simultaneously within a spray drying tower and, consequently, the drying mechanism and resultant kinetics are strongly inter-dependent on the evolving particle microstructure, [27]. To accurately describe the drying of droplets containing dissolved or suspended solids it is therefore necessary to understand their structural evolution; droplet drying simulations should be capable of describing the formation of solid particles, as well as giving the bulk moisture content. This section reviews the dried-particle morphologies observed when drying droplets in sprays together with the strategies employed to simulate these systems.
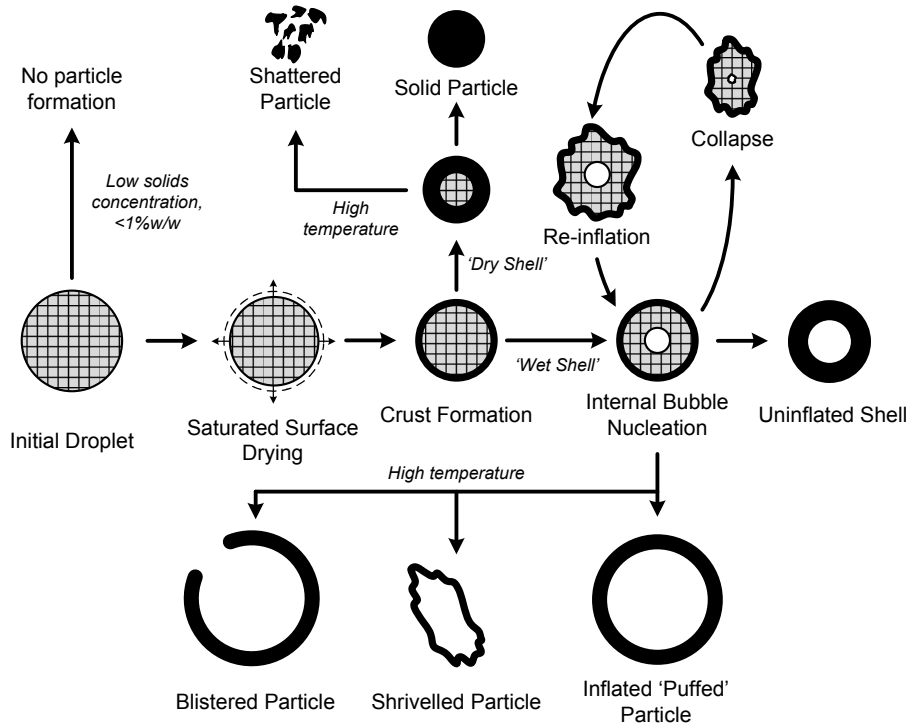
Figure 1: *Schematic showing some of the different dried-particle morphologies that may result when drying droplets containing dissolved or suspended solids.*

2.1 Dried-Particle Morphologies

Figure 1 illustrates the main dried-particle morphologies that may result when drying droplets containing dissolved or suspended solids. At very low solids concentrations, droplets continue to evaporate like pure liquid spheres and no particle is formed. However, in spray drying applications of practical interest one of the other drying routes will be followed.

Droplets initially shrink ideally in the constant rate period, but the formation of any dried-particle commences with the appearance of a surface shell. Walton and Mumford [54] identify three distinct categories of droplet, which behave in morphologically similar ways when dried: crystalline, skin-forming and agglomerate. Within these categories, the major differences in morphology following shell formation result from the drying air temperatures and, consequently, the drying rate. At lower temperatures, the mechanisms allowing for droplet shrinkage and deformation are more pronounced, [2]; moisture loss and the rate of shrinkage are slower, allowing more time for structures to deform, shrink and collapse, [39].

A solid dried-particle often forms when the drying gas temperature is below the moisture boiling point, [14]. Once a rigid crust has formed, such droplets dry somewhat like a porous solid medium with moisture menisci receding into the droplet. However, low temperature drying does not always result in the formation of solid dried-particles, [54, 55]. With aerated feeds, bubbles or voids can arise as a result of two mechanisms: the

droplet can become super-saturated with any dissolved air as a result of increasing solute concentration, [19, 20]; or entrained air pockets can coalesce and expand during drying to produce hollow particles, [53].

At high temperatures, droplets tend to inflate, form crusts and blister or break, [2]. Inflation results from large partial pressures of water vapour joining inerts in a bubble, [14, 39]. Subsequent drying behaviour and final dried-particle morphology are determined by the chemical and physical properties of the shell or film regions, [55]. For example, the rheological properties of skin-forming materials allow such droplets to undergo multiple inflation-collapse cycles. Such behaviour is observed when drying coffee extract, [8, 24] and skim-milk, [54], amongst many others. This behaviour may be contrasted with less pliable crystalline droplets that tend to undergo only partial inflation or form hollow or semi-hollow dried-particles.

2.2 Droplet Drying Models

The experimental observations discussed above show that many different dried-particle morphologies may result when drying droplets containing dissolved or suspended solids. To simulate these evolving droplet structures, it is necessary to employ spatially resolved, or mechanistic models. Three broad categories of such model may be identified: *effective diffusion* and *shrinking core* approaches, together with those *models containing a bubble*. This section reviews the many different drying models found in the literature, grouping them under these three headings.

2.2.1 Effective Diffusion Coefficient Models

Effective diffusion coefficient models assume that moisture transport within a drying droplet can be described by Fickian diffusion and, in most cases, an *effective diffusion coefficient* is required to adequately reproduce experimental results, [59]. This effective diffusion coefficient is normally a strong function of local moisture concentration and temperature and, as such, needs to be determined experimentally for each system investigated, [8, 17, 31]. There is no explicit formation of a shell region in such models, but a reduction in the effective diffusion coefficient at low moisture contents can achieve a reduction in mass transfer rate similar to that caused by shell resistance.

The effective diffusion coefficient approach is the most common method used when spatial moisture profiles are desired [*e.g.,* 18, 41, 52, 60]. However, on its own, the method yields relatively little information about droplet morphological development. For this reason, several models base their description of moisture transport on such an effective diffusion approach which they then combine with a further model for morphological changes. Some such models are discussed next.

2.2.2 Shrinking Core Models

The shrinking core model consists of two stages. Initially the droplet shrinks ideally, with solids accumulating at the droplet surface. At some point a crust is said to form, the size

of the droplet is fixed and the solution-crust interface recedes into the porous particle. Evaporation occurs at this receding interface and water must be transported to the surface by vapour diffusion through the dried shell. The mass transfer resistance of the crust therefore becomes the factor limiting the rate of continued drying.

The simplest application of the shrinking core approach assumes that the droplet outside the crust region is well mixed and, consequently, the need to track the spatial distribution of water is removed. Such models have been used to simulate droplets of sodium sulfate decahydrate [9] and coal slurries [29] amongst many others [4, 13, 38]. If spatial information on the droplet moisture content is required, a shrinking core model can be combined with an effective diffusion approach. Prior to shell formation moisture movement within the droplet is described using an effective diffusion coefficient. A dry shell subsequently grows inwards as per the shrinking core model, with an effective diffusion coefficient continuing to describe the wet core. Such an approach has been used to simulate droplets of colloidal silica, skim milk [11], an amorphous polymer solution [56] and maltodextrin [57, 58]. Nešić and Vodnik [38] presented the largest selection of experimental comparisons, investigating colloidal silica, sodium sulphate and skim milk systems.

A number of authors have published extensions to the shrinking core model. Elperin and Krasovitov [15] solved transport equations within the shell region itself whilst Seydel et al. [46] coupled such a model to a core droplet description which made use of a population balance to describe suspended solids. However, all of these models are limited in that they can only simulate predict solid dried-particles.

2.2.3 Models With a Bubble

The third class of single droplet drying model commonly found in the literature are those including a centrally located bubble. Such models allow the simulation of the hollow particles which, as discussed in Section 2.1, are often observed in practice.

Wijlhuizen et al. [60] were among the first to publish a drying model with a bubble. They postulated the presence of a bubble from the start, which could expand and contract as a result of droplet temperature variations. Sano and Keey [41] presented a model that can simulate inflation but is otherwise similar to that of Wijlhuizen et al.. Results are compared with experimental measurements of milk drying and good agreement is obtained. Hecht and King [25] presented a further model containing a bubble and used the surface tension of the shell to check the expansion of the bubble.

Minoshima et al. [36, 37] developed a relatively simple model to predict the formation of hollow granules. Their model uses the structural properties of the crust to the predict dried-particle size and shell thickness. Tsapis et al. [51] considered the electrostatic stabilisation forces between colloidal silica particles to simulate shell formation and buckling. Neither of these models simulated spatial moisture profiles, but are interesting because they demonstrate how the physical properties of droplets might be used inform the structural and morphological simulation.

2.2.4 Shortcomings of Existing Models

Whilst the single droplet drying models in the literature are generally shown to reproduce experimental mass and temperature profiles well, they are extremely limited when it comes to morphological simulation. No existing model is capable of simulating multiple dried-particle morphologies; once the use of a particular drying model has been specified, the type of dried-particle is determined. Related to this inability to predict dried-particle morphologies is the lack of any clear rational for choosing a particular model for morphological development. Given the importance of dried-particle morphology in determining the properties of spray dried-powders, the combination of these shortcomings amounts to a serious weakness in the existing models.

3 Model Review

Handscomb et al. [22, 23] introduced a new framework for simulating drying droplets, building on many of the models reviewed in the previous section. The framework, illustrated schematically in **Figure 2**, combines a core droplet description with various sub-models describing structural developments following the appearance of a surface shell. This approach means that, unlike the models discussed above, the new framework is capable of simulating multiple dried particle morphologies. This section reviews this new droplet drying; the remainder of the paper demonstrates how physically motivated criteria may be used to determine the appropriate sub-model to use following shell formation, thus allowing simulation of structural evolution as influenced by changing droplet composition and drying conditions.

3.1 Core Droplet Description

The core description permits simulation of droplets consisting of an ideal binary solution containing suspended solids. Following the convention established by Handscomb et al. [22], the solvent, solute and solid will henceforth be labelled A, B and D respectively.

3.1.1 Discrete Phase

The discrete solid phase is modelled by a population of discrete solid particles, assumed spherical and characterised by their diameter, L and radial position within the drying droplet, r. The particle number density, $N(L, r, t)$, evolved according to the population balance equation

$$\frac{\partial}{\partial t} N + \frac{\partial}{\partial L}(GN) + \frac{1}{r^2}\frac{\partial}{\partial r}\left(r^2 v_r^{(d)} N\right) - \frac{1}{r^2}\frac{\partial}{\partial r}\left(r^2 \mathrm{D}\frac{\partial N}{\partial r}\right) = 0\,, \tag{1}$$

where the evolution in physical space may occur through a convective or diffusive process. Particle growth occurs at a rate G, which is assumed to be independent of crystal
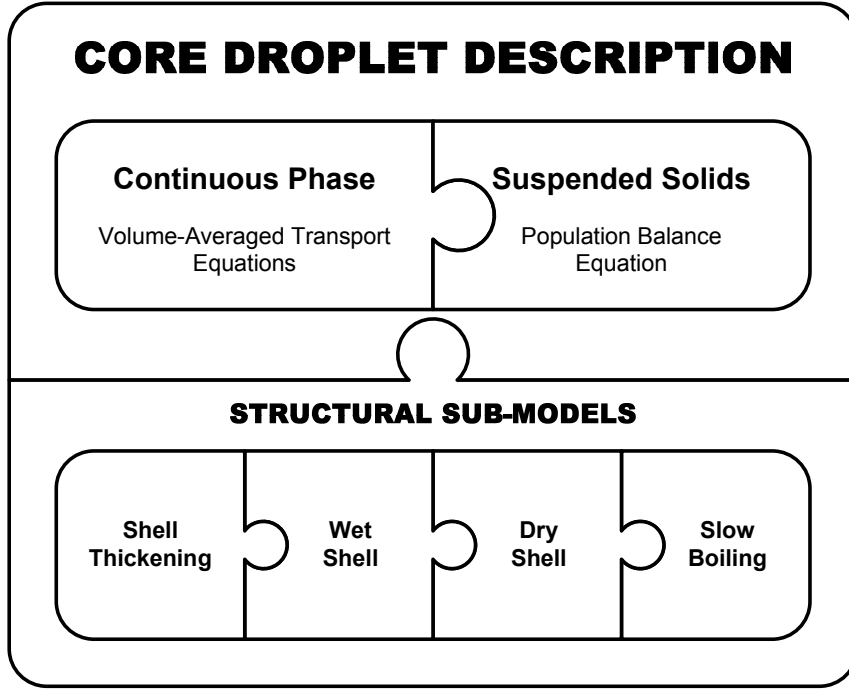
Figure 2: *Illustrating the new droplet drying framework introduced by Handscomb et al. [22, 23].*

size. Nucleation of particles of size $L_{\min}$ is accommodated through an appropriate boundary condition on the internal coordinate. Rather than solving the entire population balance equation, a moment method is employed to yield the evolution of the first four integer moments of the internal coordinate. The volume fraction of the solid phase, along with other quantities of interest, can be extracted and used to inform the predicted morphological development.

3.1.2 Continuous Phase

Modelling the continuous phase as an ideal binary solution permits its composition to be described by a single equation, derived from the volume-averaged differential mass balance for one of the species. Written in terms of the intrinsic volume average of the solute mass fraction taken with respect to the continuous phase, $\langle \omega_B \rangle^{(c)}$, the equation is

$$
\frac{\partial}{\partial t} \left[(1 - \varepsilon)\, \rho^{(c)} \langle \omega_B \rangle^{(c)} \right]
$$

$$
+ \frac{1}{r^2} \frac{\partial}{\partial r} \left[\underbrace{r^2 \, (1 - \varepsilon)\, v_r^{(c)} \rho^{(c)} \langle \omega_B \rangle^{(c)}}_{\text{advection}} - \underbrace{r^2 \mathcal{D}_{\text{eff}} \rho^{(c)} \frac{\partial}{\partial r} \left[(1 - \varepsilon)\, \langle \omega_B \rangle^{(c)} \right]}_{\text{diffusion}} \right] - r_B'' = 0 \, .
$$

$$(2)$$

$\mathcal{D}_{\text{eff}}$ is an effective diffusion coefficient usually obtained from experiments and, in general, a function of the local moisture content. r_B'' is the volume averaged interfacial production

9

rate of the solute resulting from the crystallisation process and $v_r^{(c)}$, the advective velocity, arises as a result of the density difference between the solute and solvent.

Assuming that the solute does not leave the droplet at any time, the external boundary condition on the solute equation is

$$\frac{\partial \langle \omega_B \rangle^{(c)}}{\partial r}\bigg|_{r=R} = \frac{\langle \omega_B \rangle^{(c)} \dot{m}''}{\rho^{(c)} \mathcal{D}_{\text{eff}}} \; , \tag{3}$$

where $\dot{m}''$, the solvent mass flux from the droplet surface, is given by

$$\dot{m}_{\text{vap}} = 4\pi R^2 \dot{m}'' = 2\pi \overline{\rho} \overline{\mathcal{D}}_{\text{A,air}} R \, \text{Sh}^* \log (1 + B_M) \; . \tag{4}$$

Here $\overline{\rho}$ is the density of the surrounding gas and $\overline{\mathcal{D}}_{\text{A,air}}$ is the binary diffusion coefficient of the gas and water vapour, Sh^* is the Sherwood number modified to take account of high mass transport rates from the droplet and B_M is the Spalding mass transfer number, [5, 48]. The algorithm suggested by Abramzon and Sirignano [1] is used to calculate $\dot{m}_{\text{vap}}$, together with the heat penetrating into the drying droplet. From this — and the assumption of no internal temperature gradients — the droplet temperature is evolved.

3.2   Structural Sub-Models

Within the new droplet drying framework, the structural sub-models are used in combination with the core droplet description to describe morphological evolution following formation of a surface shell. Previous drying models discussed above are only capable of simulating the morphological evolution towards one type of dried-particle. In contrast, the flexibility afforded by the new framework permits simulation of multiple dried-particle morphologies. The sub-models reviewed below are those introduced by Handscomb et al. [23], but others may be implemented to simulate other structural developments.

The *shell thickening* sub-model introduced by Handscomb et al. [23] allows for continued shrinkage of the droplet whilst the shell grows. The development of this sub-model was motivated by the observation that shell formation arrested shrinkage only for droplets forming dried-particles with a crystalline structure [54]. Such behaviour can not be described by previous droplet drying models which assume shrinkage ceases as soon as a shell is formed, [*e.g.,* 11, 29, 35].

Most drying droplets stop shrinking at some point; further moisture removal must then lead to an expanding vapour-saturated space somewhere within the droplet. In the *dry shell* sub-model the vapour space is located in the shell itself and an evaporative front recedes through the droplet. This is a variant of the classic shrinking core approach discussed in Section 2.2.2. The dry shell sub-model predicts solid dried-particles with a solids volume fraction similar to that of the droplet when it stops shrinking.

A challenge to the dry shell sub-model comes from Walton and Mumford [54], who noted that some droplets exhibit saturated surface drying throughout the shrinking period and for a short time thereafter. Such behaviour is observed even though the surface shell presents a significant obstacle to mass transfer and is in stark contrast to the behaviour predicted by the dry shell sub-model. These problems are addressed by the *wet shell* sub-model

10

wherein the shell region is assumed to be wetted by the continuous phase at all times. The vapour now lies in a single, centrally-located, bubble and evaporation proceeds from the wetted external surface. Clearly this sub-model can be used to simulate the formation of hollow dried-particles.

The *slow boiling* sub-model — the last such structural sub-model discussed by Handscomb et al. [23] — was invoked when the droplet temperature rose above the boiling point of the continuous phase. The behaviour following the start of boiling depends on the morphology of the droplet at that point. The slow boiling sub-model assumes the presence of a dry shell which is expected to be hotter than those regions still wetted by the continuous phase; it is therefore reasonable to assume that boiling commences at the evaporative front. The pressure increase at this front may influence the boiling temperature, but the slow boiling sub-model assumes that the pressure rise is insufficient to cause the droplet to crack or shatter.

If the boiling condition is satisfied prior to shell formation, or during the wet shell or thickening regimes, vaporisation is expected to commence within the drying droplet. This results in bubble formation and droplet inflation or puffing. Implementation of a sub-model to simulate drying during inflation will be discussed in a future paper. However, the model as presented in this paper can indicate when such inflation is likely to occur. Furthermore, it is noted that the new model framework discussed herein lends itself to future incorporation of such a sub-model; the infrastructure to handle an expanding, centrally located bubble has been incorporated during implementation of the wet shell sub-model.

4 Picking A Sub-Model To Use Following Shell Formation

The incorporation of several structural sub-models within the new droplet drying framework permits the simulation of multiple dried-particle morphologies. However, harnessing the potential of this approach requires the existence of criteria for picking the appropriate sub-model to apply at each stage of the droplet drying history. Structural developments may then be simulated as influenced by evolving droplet composition and changing drying conditions rather than — as was the case with all previous models — having to specify the drying route from the start. The required criteria are developed in this section, informed by an initial discussion of the physics of drying following shell formation.

4.1 Physics of Drying Following Shell Formation

4.1.1 Pressure Drop Across Surface Menisci

At the start of the drying process, all the solid particles are completely wetted by the continuous phase as illustrated in **Figure 3a**. Once a shell has formed, the continuous phase recedes to the pore mouths and menisci form between the particles at the surface.
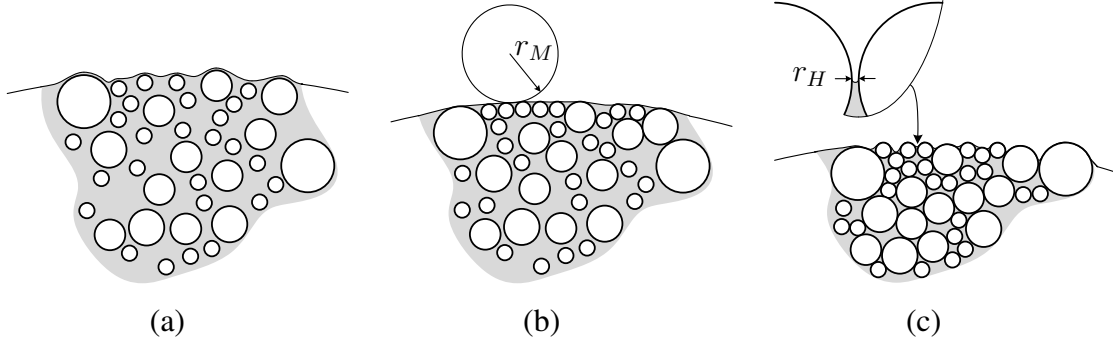
11

Figure 3: *Illustration showing the drying process in the shell thickening period. (a) Prior to shell formation, the suspended solids are completely wetted by the liquid phase. (b) On shell formation, tension develops in the liquid as surface menisci form with radii of curvature, r_M. Initially, the solid network yields easily requiring little stress to deform and, as a result, the radii of the menisci are large. (c) As the porous network stiffens, the stress required for deformation increases and the menisci radii decrease. The limiting radius — corresponding to the maximum capillary pressure — occurs when the menisci recede into the pores.*

These menisci support a pressure drop of

$$\Delta P = \frac{2\gamma}{r_M} \, , \tag{5}$$

where γ is the surface tension of the liquid phase and r_M is the radius of curvature of the meniscus. The pressure gradient within the droplet resulting from this capillary pressure leads to transport of the continuous phase towards the outer surface. At the same time, the tension from these menisci drives the solid particles past each other towards the droplet centre, [51]. These two processes occur simultaneously and — provided the capillary forces are strong enough — result in continued droplet shrinkage after the formation of a surface shell. This continued capillary driven shrinkage is termed shell thickening within this work.

During this thickening period the shell remains quite weak and the pore network shrinks in response to the capillary tension, [7]. As a result, the radius of curvature, r_M, remains large, as shown in **Figure 3b**. In some types of gel, it is possible for the pore structure to shrink to as little as one tenth of the original volume during the thickening period, [42]. However, the network will stiffen as it shrinks, increasing the capillary pressure. At some point, the radii of curvature of the surface menisci will become so small that they can fit into the pores, as shown in **Figure 3c**. This point corresponds with the start of what is sometimes termed the first falling-rate period [30] and also represents the point with the maximum capillary pressure in the liquid.

Simple geometry shows that, if the pores are assumed cylindrical, the critical radius of curvature for a meniscus entering a pore is

$$r_M = \frac{a}{\cos\theta} \, , \tag{6}$$

12

where a is the pore radius and θ is the contact angle, [42]. Clearly there will be some characteristic pore radius, r_c, corresponding to the peak capillary pressure and this will likely be related to the size of the narrowest pores. Several researchers have shown that this characteristic pore size is closely tracked by the hydraulic radius of the porous medium, [44, 47]. If the total surface area per unit volume is given by S_V, the hydraulic radius is

$$r_H = \frac{2(1-\varepsilon)}{S_V} \ . \tag{7}$$

Taking a in (6) as r_H and substituting into (5) gives the maximum pressure drop across the surface menisci as

$$\Delta P_{\mathrm{max}} = \frac{\gamma \cos \theta}{(1-\varepsilon)} S_V \ , \tag{8}$$

where the need to assume cylindrical pores has been removed. The core droplet description within the new drying framework allows the volumetric solids surface area to be obtained form the second moment of the particle number density using

$$S_V = \pi m_2 \ . \tag{9}$$

If the suspended particles are assumed to be mono-disperse with diameter L, then (7) becomes

$$r_H = \frac{(1-\varepsilon)}{3\varepsilon} L \ , \tag{10}$$

and it is seen that the characteristic pore size is inversely proportional to the solids volume fraction.

Equation (8) shows that it is theoretically possible to develop substantial pressure drops across surface menisci. As an example, consider the drying of a water based gel where the solids volume fraction, ε, is 0.65 and $S_V = 2 \times 10^8$ m^{2}m^{-3}. Water has a surface tension of 0.072 Nm^{-1} and the contact angle is taken as $\theta = 0$ rad for convenience. Under such, fairly typical, circumstances the maximum pressure drop is greater than 40 MPa.

In general, the pressure drops predicted by (8) cause a negative absolute pressure within the fluid. This implies that the drying fluid is under tension, [28]. Cavitation occurs when the negative pressure exceeds the tensile strength of the fluid, or earlier in the presence of impurities capable of acting as cavitation nuclei, [6, 49]. Cavitation is the result of the energy barrier to bubble nucleation being overcome; the result is the spontaneous appearance of a bubble within the stretched liquid, [33].

4.1.2 Pressure Drop Across a Thickening Shell

During most of the thickening period the capillary pressure is significantly less than the maximum value given by (8) and, consequently, the meniscus radius is greater than the hydraulic radius, r_H. It is therefore not possible to use (5) to directly calculate ΔP in this regime. Instead, the capillary pressure, P_{cap}, is obtained by likening the movement of the continuous phase through the shell to filtration through a porous filter with the same thickness as the growing crust, [36]. The pressure drop across the shell is then assumed equal to the pressure drop across the air–continuous phase interface. This analogy is illustrated schematically in **Figure 4**.
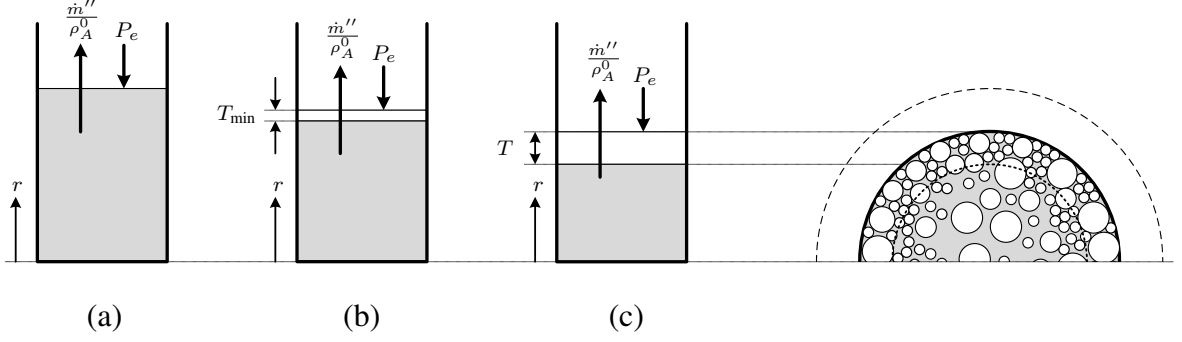
Figure 4: *Schematic demonstrating how the process of shell thickening can be likened to the growth of a filter cake: (a) Prior to shell formation; (b) the point of shell formation corresponds with the appearance of a filter cake one particle thick; (c) the filter cake thickness, T continues to increase as the shell grows. The volumetric flow through the filter cake is simply related to the mass flux from the droplet, $\dot{m}''$, and results in a pseudo-pressure acting on the shell, P_e.*

Given knowledge of the liquid flow rate, Darcy's law may be used to obtain the corresponding pressure drop across a porous medium. Darcy's Law may be written

$$\boldsymbol{q} = -\frac{\mathbf{K}}{\mu}\boldsymbol{\nabla}P \, , \tag{11}$$

where $\mathbf{K}$ is the permeability tensor for the porous body and μ is the viscosity of the flowing fluid. Assuming spherical symmetry for the drying droplets, this reduces to

$$q = -\frac{\kappa}{\mu}\frac{\partial P}{\partial r} \, , \tag{12}$$

where q is the volume flux of liquid through the shell. At the external surface, the volume flux is simply related to the mass vaporisation flux, $\dot{m}''$, by

$$q = \frac{\dot{m}''}{\rho_A^0} = -\frac{\mathrm{d}R}{\mathrm{d}t} \, . \tag{13}$$

Assuming that the problem may be analysed as a pseudo-steady state and, further, that the *total* volumetric fluid flow through the shell is not a function of radius, allows (12) to be integrated, giving

$$\begin{aligned}
\Delta P = P_R - P_S &= -\frac{\mu}{\kappa}\int_S^R \frac{\dot{m}_{\mathrm{vap}}}{4\pi r^2 \rho_A^0}\,\mathrm{d}\,r \\
&= -\frac{\mu}{\kappa}\frac{\dot{m}''}{\rho_A^0}\frac{R}{S}T \, ,
\end{aligned} \tag{14}$$

where $T = R - S$ is the shell thickness. In deriving this expression, it has also been assumed that the permeability and viscosity are constant across the thickening shell.

The permeability, κ, in (14) is estimated using the Carmen-Kozeny relation, [10],

$$\kappa = \frac{1}{180}\frac{(1-\varepsilon)^3}{\varepsilon^2}L^2 \, . \tag{15}$$

14

In the above expression, L is the diameter of the solid particles — assumed spherical and monodisperse — making up the porous medium. To account for a distribution of particle sizes, (15) may be replaced by

$$\kappa = \frac{1}{5} \frac{(1 - \varepsilon)^3}{S_V^2} \, , \tag{16}$$

where S_V is the solids surface area per unit volume, discussed above.

4.1.3 Strength of a Surface Shell

So far, this section has demonstrated a method for calculating the pressure drop that exists across the surface menisci of a droplet drying in the presence of a surface shell. This pressure drop is important as it can cause continued shrinkage of the droplet following shell formation. In order to say when the droplet *stops* shrinking, it is necessary to determine when the thickening shell becomes structurally capable of supporting itself. The continued deformation of the shell is hypothesised to occur through a series of mini-buckling events driven by the capillary pressure of the receding continuous phase. Timoshenko [50] showed that a spherical shell of radius R and thickness T will buckle when subjected to a uniform external pressure, P_{buck}, given by

$$P_{\text{buck}} = \left(\frac{T}{R - T} \right)^2 \frac{2E}{\sqrt{3 \left(1 - \nu^2 \right)}} \, , \tag{17}$$

where E is the Young's modulus of the material and ν is its Poisson's ratio. It is hypothesised that the newly formed shell will continue to experience buckling events — and therefore continue to thicken — so long as the capillary pressure is greater than the buckling pressure, P_{buck}.

4.2 Criteria for the Different Models

Having introduced the necessary theory, the criteria for applying the different sub-models following shell formation are now presented. These criteria are based on the relative magnitudes of the capillary pressure in the surface pores, the strength of the growing shell and the pressure drop across it — quantities which may be continuously tracked in the course of the simulation. The decision process applied to decide the appropriate sub-model to use is summarised in **Figure 5**; this section explores that decision process in more detail.

4.2.1 Thickening Regime

Upon formation of a surface shell, all drying droplets are assumed to enter the thickening regime. The initial shell is set to have a certain minimum thickness. Whilst this is an essentially free parameter, the diameter of the smallest solid particle sets a physical lower bound on possible shell thicknesses. The pressure drop across this shell is calculated using (14) and this will be equal to the pressure drop across the air–continuous phase
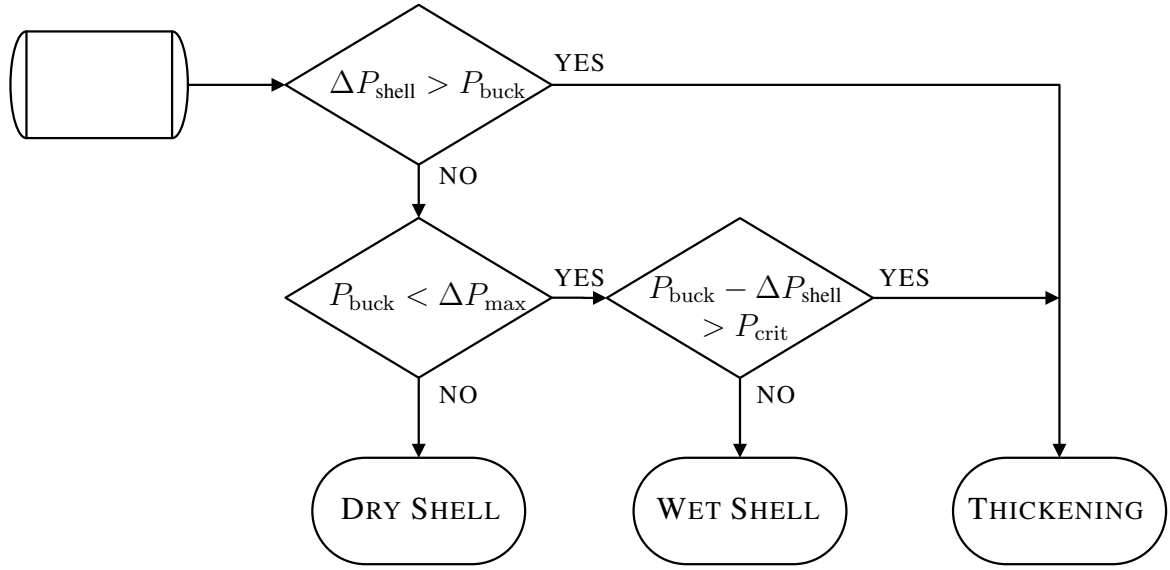
Figure 5: *Illustration of the decision process used to select the appropriate drying model to use following shell formation.*

interface. Further, the pressure required to buckle the shell, P_{buck}, is calculated using (17). As explained above, the capillary pressure in the surface pores can be thought of as exerting an external pseudo-pressure, P_e, on the thickening shell. The magnitude of this pseudo-pressure is equal to the capillary pressure at the surface which, in turn, is equal to the pressure drop across the shell. The shell will continue to thicken so long as this pseudo-pressure is greater than the pressure required to cause buckling of the shell. That is, thickening continues whilst

$$\Delta P_{\text{shell}} > P_{\text{buck}} \, , \tag{18}$$

or, on substituting from (14) and (17) and re-arranging, whilst

$$\frac{R \, (R - T)}{T} \dot{m}'' \; > \; \frac{\kappa}{\mu} \frac{2 E \rho_A^0}{\sqrt{3 \, (1 - \nu^2)}} \, . \tag{19}$$

The structural properties of the growing shell are seen to directly influence the duration of the thickening regime, as is the drying rate, $\dot{m}''$.

The thickening period extends whilst the inequality in (19) is satisfied. However, this condition is sufficient but not necessary for thickening, *i.e.,* thickening does not necessarily cease once (19) is no longer satisfied. The reason for this is that the surface menisci between suspended solid particles are potentially capable of supporting a greater pressure drop than that across the thickening shell. Once (19) is no longer satisfied, the menisci will retreat into the surface pores, reducing their radius of curvature and thus increasing the associated capillary pressure. This retreat will continue until the pressure is sufficient to cause further buckling, or until the capillary pressure exceeds the maximum possible value as given by (8).
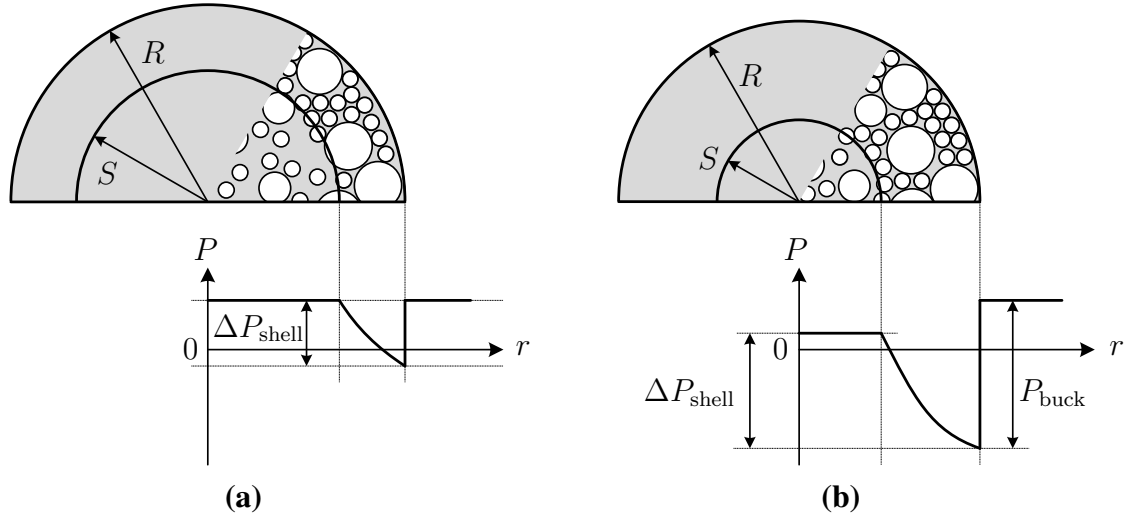
16

Figure 6: *Illustration of the pressure profiles within a drying droplet following formation of a surface shell: (a) the pressure drop across the liquid–air interface is equal to the pressure drop across the shell, ΔP_{shell} when this is greater than the buckling pressure, P_{buck}; (b) when $P_{\text{buck}} > \Delta P_{\text{shell}}$, the pressure drop across the interface is equal to the buckling pressure and the pressure in the droplet core falls below ambient.*

Thickening will cease once the capillary pressure exceeds the maximum possible value, ΔP_{max}. At this point, the menisci retreat beneath the surface and the dry shell regime commences. However, it is possible for the thickening regime to end earlier by progression to the wet shell regime.

4.2.2 Wet Shell Regime

When drying droplets with a surface shell, the surface menisci support a pressure drop across the air-continuous phase interface. As explained above, it is initially assumed that this pressure drop is equal in magnitude to the pressure drop across the thickening shell and, consequently, the pressure profile in the drying droplet is similar to that sketched in **Figure 6a**. Once the menisci begin retreating into the surface pores, the pressure drop across the menisci grows larger than that across the shell. As a result, the fluid pressure in the core region falls below atmospheric, as illustrated in **Figure 6b**.

The wet shell sub-model postulates the growth of a centrally located vapour-saturated bubble within the drying droplet. This approach is clearly a gross simplification of the physics occurring within a real drying droplet, but it is possible to motivate the idea of a centrally located bubble in a number of ways. Firstly, dissolved gases present in the initial droplet may come out of solution to form bubbles, or small bubbles may even be present in the initial feed. As the pressure in the droplet falls, these bubbles will expand. In the absence of such features, cavitation will occur when the pressure falls below the vapour pressure of the liquid by an amount dictated by the tensile strength, (§4.1.1). However the bubble forms in a particular system, the present drying model postulates that a droplet will cease thickening and enter the wet shell regime once $P_{\text{buck}} - \Delta P_{\text{shell}} < P_{\text{crit}}$, where P_{crit} is some critical pressure. The complete process for deciding the relevant drying regime is

illustrated in **Figure 5**.

4.2.3 Wet Shell to Dry Shell Switch

As mentioned above, the dry shell model can directly follow the thickening regime when $P_{\text{buck}} > \Delta P_{\text{max}}$. This is likely to occur for droplets containing large suspended solids, *e.g.,* the detergent crutcher mix droplet simulated by Handscomb et al. [23] where direct progression to the dry shell regime was presumed. However, it is also possible that the dry shell regime might be entered following a period of wet shell drying.

The wet shell model includes an expanding central vapour space with a slowly growing outer shell. It is clear that if this regime persist for a sufficiently long time, the growing bubble will meet the retreating inner shell surface. At this point, the bubble can expand no more and further moisture removal necessitates drying of the shell itself. In general, it is possible that the switch between the wet and dry shell drying regimes might occur before this point. Such an eventuality leaves three spatial domains: a region adjacent to the bubble, formerly the wet core; a region corresponding to the previous wet shell; and the new, growing, dry shell region.

5   Results

The new droplet drying framework is now applied to investigated the drying of a droplet of aqueous colloidal silica. Walton and Mumford [54] identified colloidal silica as a material where droplets were found to continue shrinking upon drying, even after the formation of a surface shell. Furthermore, it was observed that moisture is removed by saturated surface drying throughout this shrinking period and that this continues for a short while after the droplet size has stabilised. Such behaviour suggests that this system is a good candidate for demonstrating the shell thickening and wet shell sub-models. The same system was simulated by Handscomb et al. [23], but in the present paper the new criteria for selecting structural sub-models are employed to investigate the sensitivity of dried-particle morphology to suspended particle size.

5.1   Base Case

The base case consists of a droplet containing 16 nm colloidal silica particles suspended in water. To simulate this system within the new droplet drying framework the solute mass fraction is initialised to a very small number, 10^{-9}, thus approximating the pure water continuous phase. Gelation occurs as the concentration of colloidal silica is increased and, in the system simulated here, this is seen to occur at mass fractions above 40wt%.

5.1.1 Physical Properties

Nešić and Vodnik [38] report that the solids diffusion coefficient in the gel phase is

$$D = \exp\left(-\frac{28.1 + 282\,\omega_A}{1 + 15.47\,\omega_A}\right) \, , \tag{20}$$

where $\omega_A = 1 - \omega_D$ is the mass fraction of water. Prior to gel formation — that is, at solids volume fractions below 0.23 — experimental observations suggest that internal convection currents keep the drying droplets well mixed, [38]. To simulate this, the solids diffusion coefficient is set to 10^{-7} $m^2 s^{-1}$ — a relatively large value — at low solids concentrations. The discontinuity at the point of gel formation was found to cause problems for the numerical solution routine and so was smoothed using a hyperbolic tangent weighting function. The expression used for the solids diffusion coefficient is therefore

$$D\left(\omega_D\right) = f\left(\omega_D\right) \times 10^{-7} + \left(1 - f\left(\omega_D\right)\right)\exp\left(-\frac{28.1 + 282\left(1 - \omega_D\right)}{1 + 15.47\left(1 - \omega_D\right)}\right) \, , \tag{21}$$

where

$$f\left(\omega_D\right) = \frac{1}{2}\left[1 - \tanh\left(20\pi\left(\omega_D - 0.35\right)\right)\right] \, . \tag{22}$$

Investigations reported by Handscomb [21] suggest that the appropriate sorption isotherm to use is

$$p_{A,\mathrm{sur}} = p_A^{\mathrm{sat}}\left(1 - \exp\left(-5\omega_A\right)\right) \, , \tag{23}$$

which was obtained by fitting the simulated results to experimental observations prior to shell formation. This isotherm refers to evaporation from a fully wetted surface and, consequently, the Kelvin equation is applied to account for the vapour pressure reduction that results as the surface menisci begin to retreat into the pores of the newly formed shell. The resulting correction was found to be insignificant.

As explained in Section 4.1.3, the Young's modulus and Poisson's ratio of the colloidal silica shell are required to model moisture removal and dried-particle formation following the appearance of a surface shell. Smith et al. [47] measured the shear modulus of wet silica gels, from which the Young's modulus can be calculated, given knowledge of the Poisson's ratio, ν. Taking $\nu = 0.2$, as was measured by Scherer [43] for similar silica gels, gives the estimated Young's modulus for the system as 1 MPa. This is relatively low, suggesting that the shell should be expected to buckle repeatedly as the droplet dries, leading to considerable thickening.

The method described in Section 4.2 is used to select the appropriate model to use as the droplet dries. To apply this methodology two parameters are needed in addition to those describing the structural properties of the shell. The first of these is the liquid-solid contact angle, θ, for use in (8). Asmatulu [3] reports a range of possible values, depending on the hydrophobicity of the silica particles used. Hunter et al. [26] give a value of $37°$, obtained by averaging the results obtained from a number of experimental methods. This is in broad agreement with the contact angles given by Asmatulu for silica particles with no added cleaning agents and so this is the value taken for the present set of simulations.

The second remaining parameter is P_{crit}, the critical pressure which determines when a droplet will cease thickening and enter the wet shell regime, (see Figure 5). By coincidence, it is found that P_{crit} is not required for the base case when simulating droplets containing 16 nm particles. This is because the drying droplet is predicted to enter the dry shell regime directly following shell thickening, thus avoiding a wet shell drying period. However, in general, this parameter must be assigned a value and a method for doing this is discussed below.

When the growing bubble meets the internal boundary of the wet shell region, the model switches from the wet to dry shell mode as discussed in Section 4.2.3. The dry shell tortuosity, σ, used when calculating the mass vaporisation rate is taken as 10 m m^{-1}. This is based on the crust diffusion coefficient reported by Nešić and Vodnik [38] for the system simulated here. When the temperature of the droplet reaches $100°$C, the remaining water will boil. Given long enough in the dryer, all the remaining water will be vaporised and the temperature of the dried-particles will rise to that of the drying air.

5.1.2 Comparison with Experimental Data

Direct comparisons with the experimental data of Nešić and Vodnik [38] at $T_{\text{gas}} = 101°$C and $T_{\text{gas}} = 178°$C are presented for the base case in **Figure 7 (a)** and **(b)** respectively. Following the findings of the investigations reported by Handscomb [21], the drying air is here assumed to be dehumidified and moving with a velocity of 2.5 ms^{-1} relative to the droplet. A shell is deemed to have formed once the solids volume fraction at the droplet surface exceeds 0.65.

At both temperatures, the agreement between the predicted droplet mass and that measured experimentally is very good throughout the drying history. For the droplet drying in air at $101°$C, the modelled temperature under-predicts the experimentally measured value following the formation of a shell at $t = 58.2$ s. It is likely that this discrepancy is caused by the assumption of a uniform droplet temperature, even after the formation of a dry shell at $t = 70.2$ s. Indeed, it is within this dry shell period that the temperature discrepancy is most pronounced. In reality, it is expected that a dried shell region will be hotter than the still-wet core; Farid [16] goes so far as to suggest the temperature in this region will equal that of the drying gas, although this is strongly disputed by Schlünder [45]. Nevertheless, it seems likely a dry shell region will be somewhat warmer than the core and, furthermore, that the experimental thermocouple readings will reflect the presence of this hotter region. Consequently, it is perhaps not surprising that the measured droplet temperatures are higher than those predicted by the model as a result of the uniform temperature assumption.

Figure 7 (b) shows the results for a colloidal silica droplet drying in air at $178°$C. As the air temperature is above the boiling point of water, it is expected that this droplet will undergo boiling; this is immediately clear from the figure. The switch to dry shell drying, occurs at $t = 33.2$ s, at which point the droplet temperature begins to rise rapidly. At $t = 35.5$ s, when the temperature reaches $100°$C — the boiling point of water — the slow boiling regime is said to commence, (§3.2). The remaining water in the droplet is removed by boiling, during which time the temperature remains constant. Once all the moisture has been removed, at $t = 41.4$ s, the droplet mass ceases to decrease and the temperature
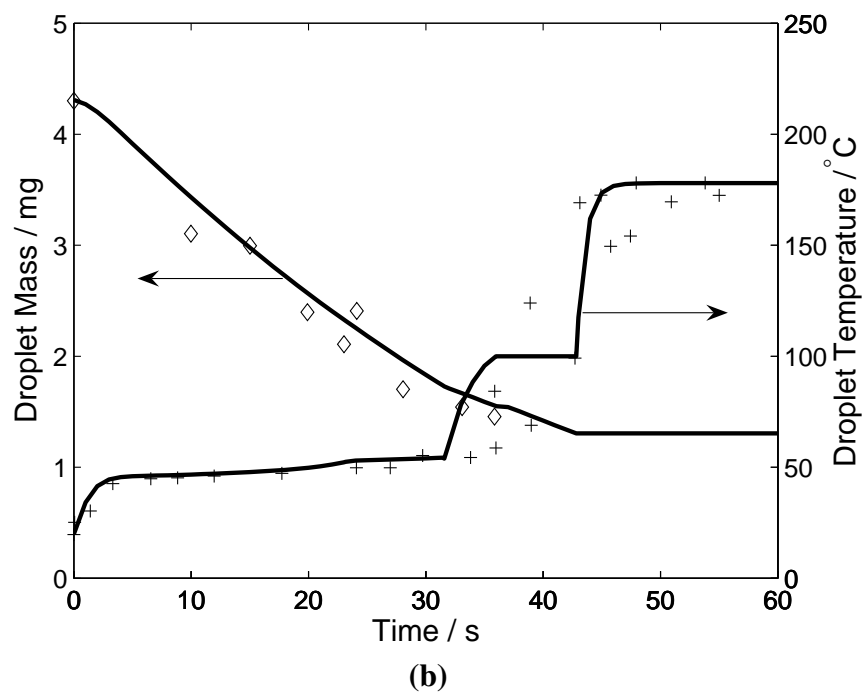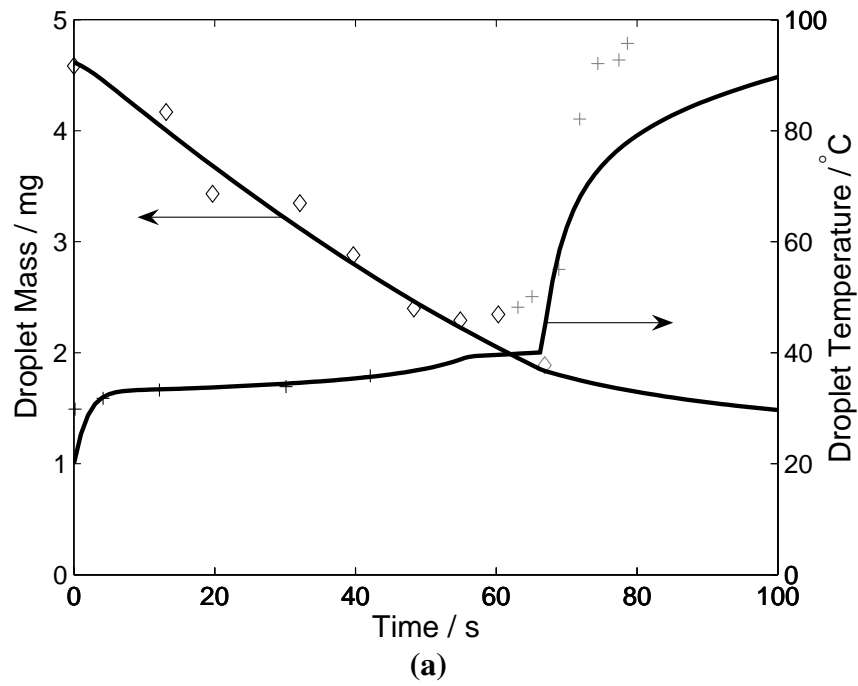
Figure 7: *Simulated drying of a colloidal silica droplet (lines) compared with experimental results from Nešić and Vodnik [38] (symbols) at: (a) $T_{\text{gas}} = 101°C$ and $R_0 = 0.972$ mm; and (b) $T_{\text{gas}} = 178°C$ and $R_0 = 0.95$ mm.*

rises to that of the drying air.

The prediction of the droplet temperature for this example is seen to be in very good general agreement with the experimentally observed values. It is noted that there is a fair degree of scatter in the measured values following the predicted formation of a dried shell. As discussed in relation to the results at the lower air temperature, this could reflect the thermocouple variously returning readings reflecting the temperature in the still-wet core or the hotter, dried shell. However, the general timescale over which the droplet temperature rises to that of the drying gas is correct and, given the nature of the model, the predicted profiles make good sense.

5.1.3 Structural Development

As discussed in Section 4, the various pressure drops within the drying droplet are key to determining its evolving structure. **Figure 8** shows the evolution of the buckling pressure, P_{buck}, the pressure drop across the shell, ΔP_{shell} and the maximum pressure drop that can be supported across the surface menisci, ΔP_{max}. For an array of 16 nm particles, the hydraulic radius — approximating the minimum pore size — as given by (10) is 2.87 nm, where the solids volume fraction is assumed to be 0.65. Using (5) with $\theta = 37°$ shows the surface menisci in this system can support a pressure drop of over 40 MPa. Also shown in the figure is the pressure in the wet core although, in this example, this does not change during the thickening period. This figure can be used in conjunction with Figure 5 to determine the morphological progression of the drying droplet. The pressure drop across the shell is significantly greater than that required for buckling at all times. Thickening therefore continues until the pressure drop across the shell equals ΔP_{max}, which is seen to occur at $t = 33.0$ s. At this point the menisci retreat into the surface pores and, consequently, the droplet is predicted to pass directly from the thickening to the dry shell regime.

Figure 9 shows the simulated structural evolution of the droplet drying in air with $T_{\text{gas}} = 178°$C. The different drying regimes are clearly visible and it is possible to see the morphology of the droplet at a given time in the drying history. Thickening commences at $t = 24.4$ s, after which the wet shell thickens considerably before, as just discussed, passing directly into the dry shell regime at $t = 33.0$ s. At this point of transition the droplet has a region of still-wet core of radius 0.227 mm surrounded by a thickened shell region extending out to the external radius at $R = 0.599$ mm. Once the dry shell regime has commenced there are, in effect, three domains: the wet core; the thickened shell; and the dry shell region. Rather than explicitly modelling three spatial domains, this situation is handled here by setting the solids diffusion coefficient equal to zero in the thickened shell — that is, particles in the thickened shell are not free to move during the dry shell regime. A dried-particle is said to have formed once all the moisture has been removed from the droplet — this occurs after 41.7 s.

Figure 10 shows the simulated evolution of the solids volume fraction within the droplet of colloidal silica, drying with $T_{\text{gas}} = 178°$C. Profiles are plotted at 5 s intervals. Initially these profiles are flat across the droplet due to internal circulation prior to gelation. After formation of a gel at $\varepsilon = 0.233$, the profiles develop a pronounced curvature as particles build up at the receding interface. The profile shown in bold is that at $t = 24.4$ s when
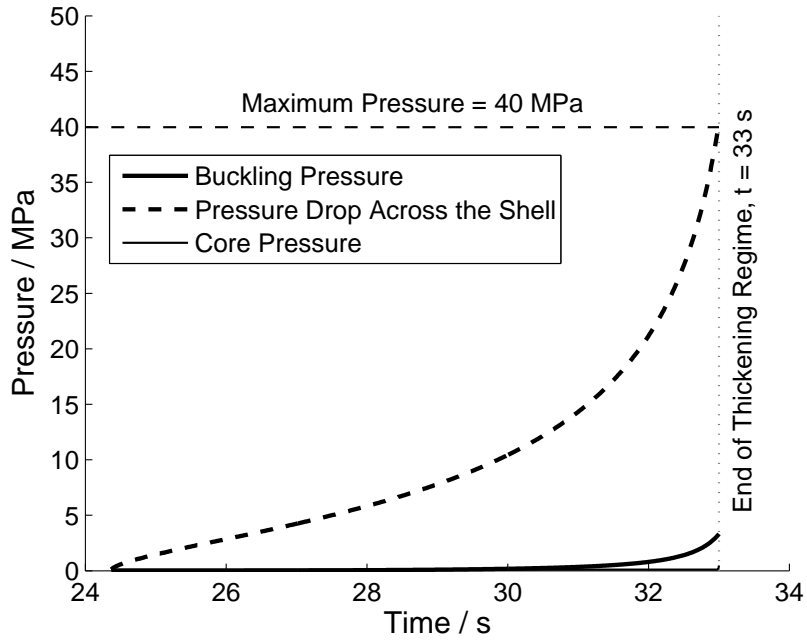
22

Figure 8: *Plot showing various pressures relating to a droplet of colloidal silica drying in air at* $T_{\mathrm{gas}} = 178°C$ *during the shell thickening regime. The suspended silica particles have a diameter of* 16 nm.
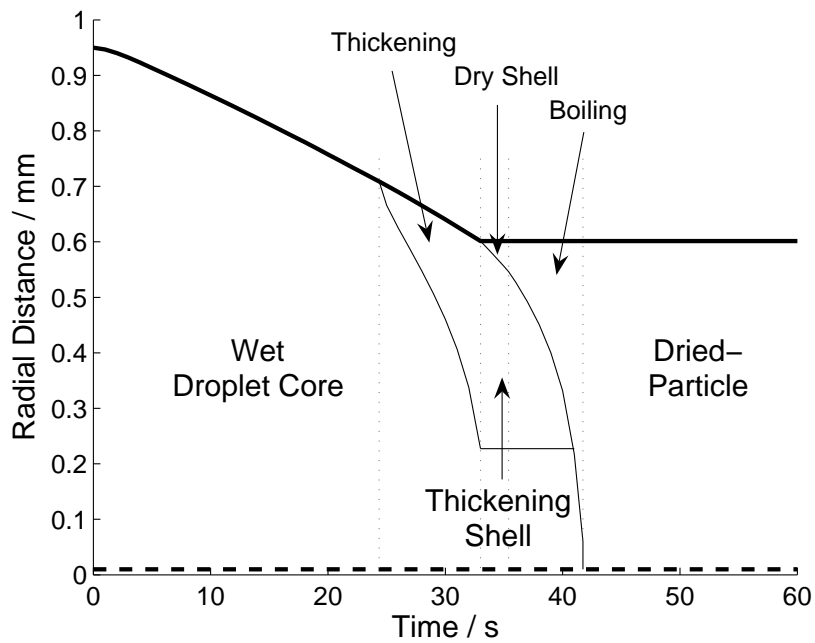

Figure 9: *Simulated morphological evolution of a droplet of colloidal silica containing* 16 nm *particles drying in air at* 178°C.
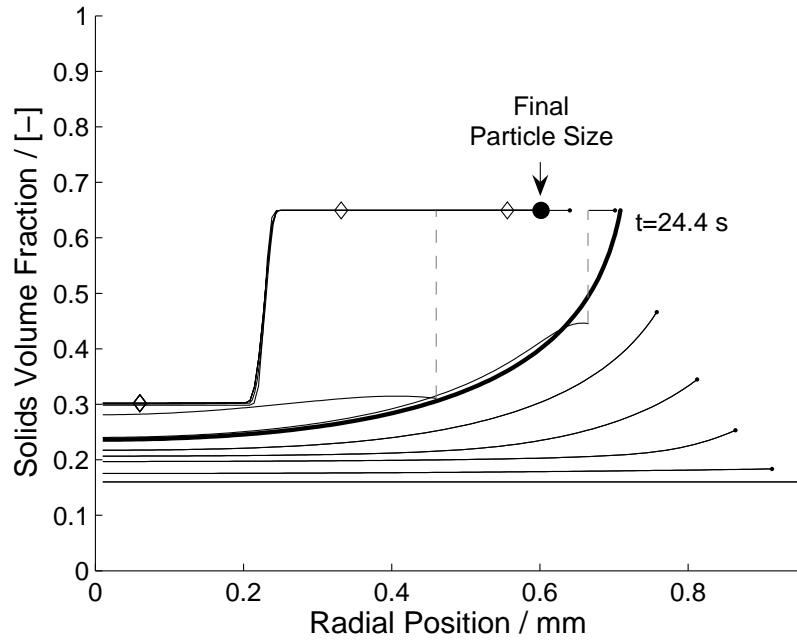
Figure 10: *Simulated solids volume fraction profiles during the drying of a colloidal silica droplet containing 16 nm particles drying in air at $T_{\text{gas}} = 178°C$. Profiles are plotted at 5 s intervals, with the $t = 24.4$ s profile at the point of shell formation highlighted in bold. The external radius of the droplet is shown on each profile as a small dot; a larger dot represents the final particle size. The diamonds on the later profiles show the position of the evaporative front during the dry shell regime.*

the solids volume fraction at the surface reaches 0.65 and the shell forms. After this, the droplet continues to shrink whilst the shell thickens. The solids volume fraction in this shell region is 0.65 whilst the fraction in the core region is considerably less. This is clear from the two profiles with discontinuities taken during the thickening regime.

The interface at $r = 0.227$ mm between the wet core and thickened shell regions is clear in the later profiles plotted in Figure 10. This is a result of the direct transition between the thickening and dry shell regimes, discussed above. Bypassing a wet shell drying period means that the resulting dried-particle is predicted to be solid but, as is clear from Figure 10, the central region is expected to have a considerably lower solids content.

Although not presented here, the droplet drying in air at $T_{\text{gas}} = 101°C$ is predicted to have a very similar morphology to that outlined above. The main reason for this is the small size of the suspended solid particles, leading to high pressure drops across the thickening shell as well as large maximum pressure drops across the surface menisci.

5.2 Effect of Suspended Particle Size

The newly developed criteria for picking the structural sub-model to apply following shell formation permit investigation of the morphologies that might result from similar suspen-
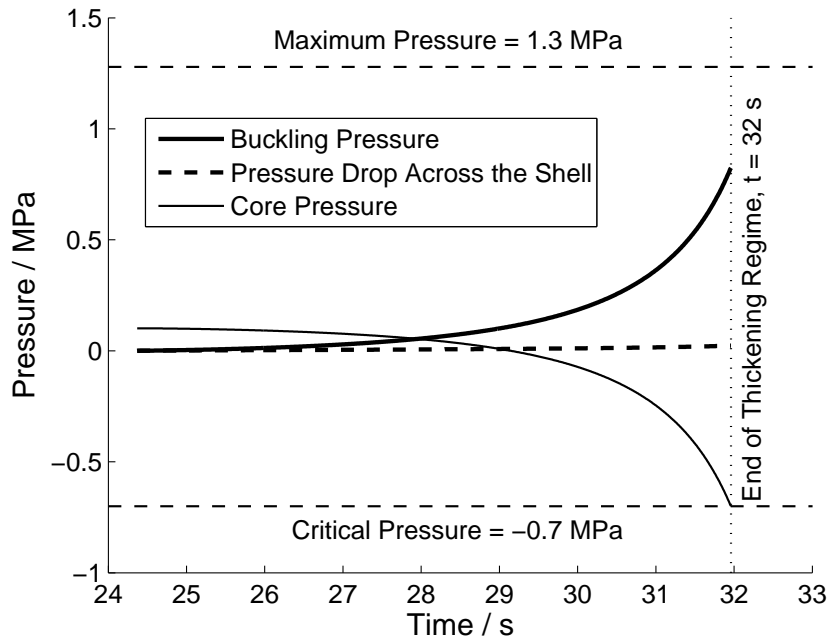
Figure 11: *Plot showing various pressures relating to a droplet of colloidal silica drying in air at $T_{\text{gas}} = 178°C$ during the shell thickening regime. The suspended silica particles have a diameter of 500 nm.*

sions of larger particles. To do this, it is assumed that other properties of the droplet remain constant — in particular, the solids diffusion coefficient and gelling concentration are unchanged. This is likely to be un-physical, but does not prevent qualitative conclusions being drawn.

The pressure profiles during the thickening regime for a droplet containing 500 nm particles are shown in **Figure 11**. Comparison with Figure 8 immediately demonstrates some major differences. Firstly, the pressures involved are considerably lower; the maximum pressure drop across the surface menisci for a droplet with 500 nm particles is 1.3 MPa compared with the figure of 40 MPa for the previous droplet. Further, the pressure drop across the shell is now seen to be less than that required for buckling. However, thickening continues as P_{buck} is itself initially less than the maximum pressure drop across the air-liquid interface. The interesting line on this plot is that indicating the pressure in the droplet core, *i.e.,* inside the thickening shell. This is seen to fall during the thickening regime with negative values indicating a negative absolute pressure within the droplet.

Reference to Figure 5 shows that the thickening regime can end if the core pressure falls below a certain critical value, P_{crit}. This is indicated on Figure 11, where it is seen that this is indeed the manner in which shell thickening is halted for this droplet. The choice of the critical value is far from clear and, essentially, this may be thought of as a free parameter. In the present example, the value $P_{\text{crit}} = -0.7$ MPa was chosen for reasons explained below.

Figure 12 shows the structural evolution of the hypothetical droplet containing 500 nm silica particles. It is instructive to compare this with Figure 9, the analogous plot for the
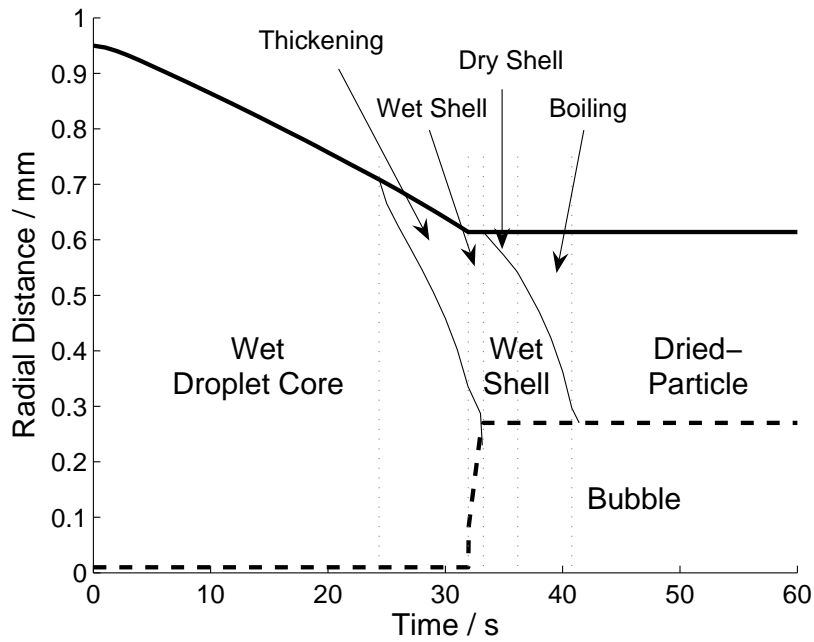
Figure 12: *Simulated morphological evolution of a droplet of colloidal silica containing* 500 nm *particles drying in air at* $178°$C.

droplet containing 16 nm particles. The droplet with larger particles is seen to undergo a period of wet shell drying and, consequently, the resulting dried-particle is hollow. This is clearly seen in **Figure 13**, which shows the simulated evolution of the solids volume fraction within the droplet containing 500 nm particles. The central bubble is clearly visible and close comparison with Figure 10 shows that a larger dried-particle is predicted.

Clearly the size of the suspended particles influences the drying modes and, consequently, the morphology of the final dried-particle. **Figure 14** illustrates this link more clearly, combining the results of many simulations to produce a map showing the drying routes of droplets containing various sizes of suspended particles. For droplets containing small particles — like the first droplet simulated in this section — solid dried-particles result with no wet shell drying period. Droplets containing solid particles between 50 and 1000 nm in diameter pass through a wet shell region in their drying histories and, as a result, produce hollow dried-particles. However, for droplets with suspended particles larger than 1 μm, the wet shell region is again bypassed and solid dried-particles are produced.

The existence of a transition from hollow back to solid dried-particles as suspended particle size increases is the key to choosing the critical pressure that determines the start of the wet shell drying regime, P_{crit}. Walton and Mumford [54] observed a range of colloidal silica droplets drying and reported that solid dried-particles tended to be formed when the suspended solids were larger than 1 μm in size, with hollow dried-particles resulting from droplets containing smaller suspended solids. Bearing this result in mind, P_{crit} was set equal to -0.7 MPa in these simulations to ensure the transition from hollow to solid particles occurs at the correct suspended particle size.
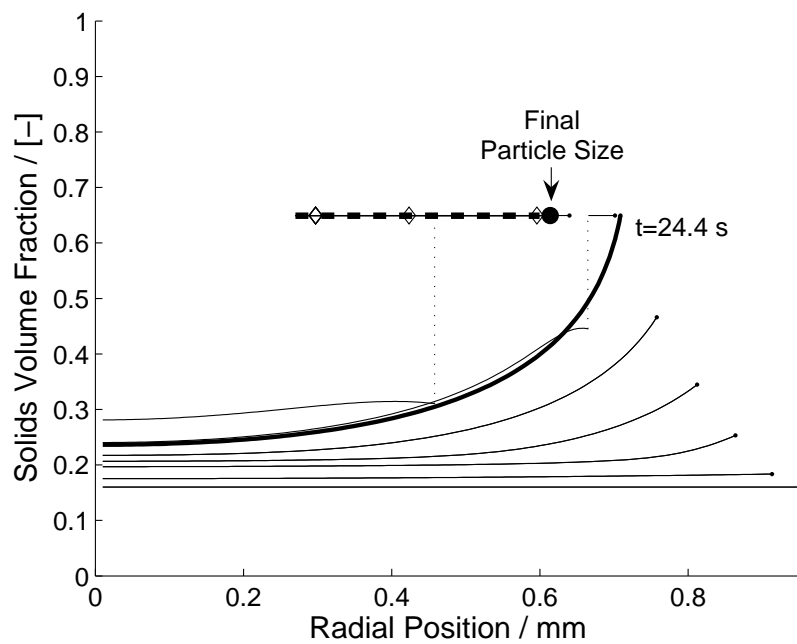
Figure 13: *Simulated solids volume fraction profiles during the drying of a colloidal silica droplet containing 500 nm particles drying in air at $T_{\text{gas}} = 178°C$. Profiles are plotted at 5 s intervals, with the $t = 24.4$ s profile at the point of shell formation highlighted in bold. The external radius of the droplet is shown on each profile as a small dot; a larger dot represents the final particle size. The diamonds on the later profiles show the position of the evaporative front during the dry shell regime. The solids profile in the dried-particle is shown by the heavy dashed line.*

Figure 14: *Schematic showing the effect silica particle size on the predicted drying process.*
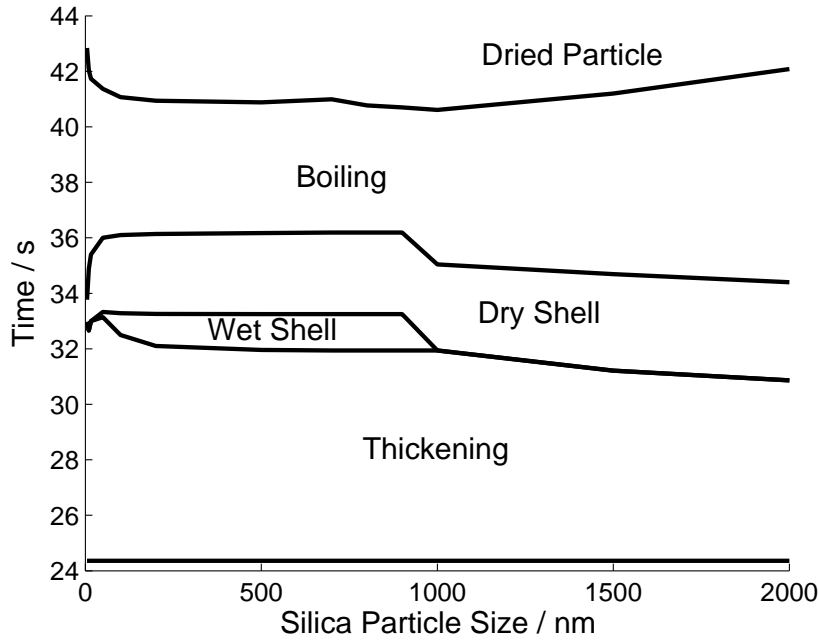
Figure 15 shows the pressure profiles in the thickening regime for a drying droplet containing suspended particles 1500 nm in diameter. Such droplets are predicted to form solid dried-particles — that is, they bypass the wet shell drying period. The reason for this is clear from the pressure profiles. With the pressure drop across the shell less than the pressure required for buckling, it is the later which determines the pressure drop across the air–liquid interface, (§4.1). For this droplet, the constraint that this pressure must be less than ΔP_{max} is seen to be binding, *i.e.,* the buckling pressure exceeds the maximum pressure capable of being supported by the surface menisci before the core pressure falls below the critical value, P_{crit}. Reference to Figure 5 shows that this sequencing results in direct transition to the dry shell drying regime.

6   Conclusion

This paper built on the new droplet drying framework developed by Handscomb et al. [22, 23]. This framework combines a core droplet description with a number of structural sub-models to describe the droplet evolution following formation of a surface shell. The focus of this paper was developing criteria for choosing the appropriate structural sub-model to use at any point throughout the drying history.

Experimentally observed dried-particle morphologies were discussed, together with a thorough review of spatially resolved, mechanistic drying models from the literature. It is noted that all existing models require the drying route to be specified *a priori* and, consequently, they are only capable of simulating a single structural history. Before a single mechanistic drying model is able to simulate multiple dried-particle morphologies, it is
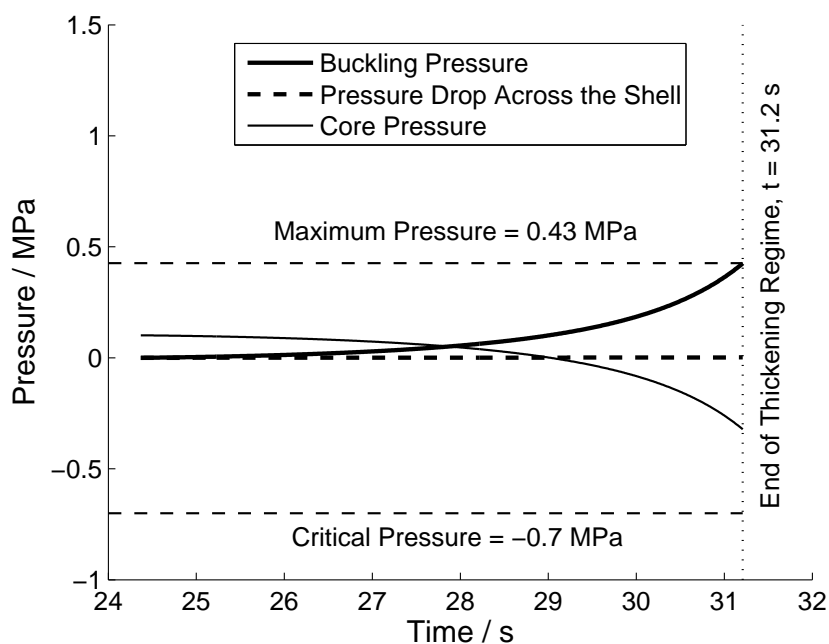
28

Figure 15: *Plot showing various pressures relating to a droplet of colloidal silica drying in air at* $T_{\text{gas}} = 178°C$ *during the shell thickening regime. The suspended silica particles have a diameter of* 1500 *nm.*

necessary to develop on-line criteria to decide the appropriate sub-model to use at any stage of the drying history. To this end, the physics of droplets drying in the presence of a surface shell were studied, focusing of pressure changes within the shell region. The resulting understanding enabled the development of physically motivated criteria for picking a structural sub-model, thus allowing simulation of structural evolution as influenced by changing droplet composition and drying conditions.

The new criteria were demonstrated by using the droplet drying framework to simulate a droplet of colloidal silica. Temperature and mass histories from the base case simulation were compared with experimental data, with which they showed good agreement. A parameter study was then performed to investigate the influence of suspended particle size on final dried-particle morphology. In simulating these droplets, all the structural sub-models were used as dictated by application of the newly developed decision criteria. Combining the results from multiple simulations allowed production of a map illustrating the link between suspended particle size and dried-particle morphology. This demonstrates that, for the first time, a single mechanistic droplet drying model is capable of simulating multiple dried-particle morphologies.

29

Nomenclature

Greek Characters

γ	Surface tension	[N·m^{-1}]
ε	Solids volume fraction	[-]
$\varepsilon_{\mathrm{crit}}$	Critical solids volume fraction triggering shell formation	[-]
θ	Contact angle	[deg] or [rad]
κ	Permeability	[m^2]
μ	Viscosity	[Pa·s]
ν	Poisson's ratio	[-]
ρ	Mass density	[kg·m^{-3}]
ρ_j^0	Material density of component j	[kg·m^{-3}]
σ	Tortuosity	[-]
ω_j	Mass fraction of component j, (liquid phase)	[-]

Operator

$\langle B \rangle^{(i)}$	Intrinsic volume average of B associated with phase i

Roman Characters

B_M	Spalding mass transfer number	[-]
D	Solids diffusion coefficient	[m^2 s^{-1}]
$\mathcal{D}_{\mathrm{eff}}$	Effective diffusion coefficient	[m^2 s^{-1}]
E	Young's modulus	[Pa]
G	Linear growth rate	[m·s^{-1}]
K	Permeability tensor	[m^2]
L	Internal coordinate – solid particle diameter	[m]
M	Droplet mass	[kg]
N	Number density function	[# m^{-4}]
P	Pressure	[Pa]
P_{cap}	Capillary pressure	[Pa]
P_{crit}	Critical pressure determining the onset of wet shell drying	[Pa]
P_e	External pseudo-pressure acting on a growing shell	[Pa]
R	Radius of the drying droplet	[m]
S_V	Surface area per unit volume	[m^{2}m^{-3}]
Sh*	Modified Sherwood number	[-]
T	Shell thickness	[m]

T_{boil}	Boiling temperature of the continuous phase	[°C] or [K]
T_d	Droplet temperature	[°C] or [K]
V	Volume	[m^3]
a	Pore radius	[m]
$\dot{m}''$	Mass vapour flux from the droplet	[kg·m^{-2}s^{-1}]
$\dot{m}_{\text{vap}}$	Total rate of solvent evaporation	[kg·s^{-1}]
p	Partial pressure	[Pa]
$\boldsymbol{q}$	Volumetric flow rate	[m^{-3}s^{-1}]
r	Internal coordinate – radial position	[m]
r''	Volume average interfacial production rate	[kg·m^{-2}s^{-1}]
r_c	Characteristic pore radius	[m]
r_M	Radius of curvature	[m]
t	Time	[s]
v_r	Radial velocity	[m·s^{-1}]

Superscripts and Subscripts

A	Solvent
B	Solute
D	Solids
buck	The buckling condition
c	Continuous phase
d	Discrete phase

References

[1] B. Abramzon and W. A. Sirignano. Droplet vaporization model for spray combustion calculations. *International Journal of Heat and Mass Transfer*, 32(9):1605–1618, 1989. doi:10.1016/0017-9310(89)90043-4.

[2] L. Alamilla-Beltrán, J. J. Chanona-Pérez, A. R. Jiménez-Aparicio, and G. F. Gutiérrez-López. Description of morphological changes of particles along spray drying. *Journal of Food Engineering*, 67(1-2):179–184, March 2005. doi:10.1016/j.jfoodeng.2004.05.063.

[3] R. Asmatulu. Enhancement of the dewetability characteristics of fine silica particles. *Turkish Journal of Engineering and Environmental Sciences*, 26(6):513–520, November 2002.

[4] T. O. K. Audu and G. V. Jeffreys. The drying of drops of particulate slurries. *Transactions of the Institution of Chemical Engineers*, 53:165–172, 1975.

[5] R. B. Bird, W. E. Stewart, and E. N. Lightfoot. *Transport Phenomena*. John Wiley and Sons, 1st edition, 1960.

[6] L. J. Briggs. Limiting negative pressure of water. *Journal of Applied Physics*, 21(7): 721–722, July 1950. doi:10.1063/1.1699741.

[7] C. J. Brinker. *Sol–Gel Processing of Silica*, volume 131 of *Surfactant Science Series*, chapter 47, pages 615–635. CRC Press, Taylor and Francis Group, 6000 Broken Sound Parkway NW, Suite 300 Boca Raton, FL 33487-2742, 2006.

[8] D. H. Charlesworth and W. R. Marshall. Evaporation from droplets containing dissolved solids. *AIChE Journal*, 6(1):9–23, 1960. doi:10.1002/aic.690060104.

[9] H. Cheong, G. Jeffreys, and C. Mumford. A receding interface model for the drying of slurry droplets. *AIChE Journal*, 32(8):1334–1346, August 1986. doi:10.1002/aic.690320811.

[10] J. M. Coulson, J. F. Richardson, J. R. Backhurst, and J. H. Harker. *Coulson and Richardson's Chemical Engineering: Particle Technology and Separation Processes v. 2*. Coulson and Richardson's Chemical Engineering. Butterworth-Heinemann Ltd, 4th edition, 1996.

[11] N. Dalmaz, H. O. Ozbelge, A. N. Eraslan, and Y. Uludag. Heat and mass transfer mechanisms in drying of a suspension droplet: A new computational model. *Drying Technology*, 25(2):391–400, February 2007.

[12] W. H. de Groot, L. Adami, and G. F. Moretti. *Manufacture of Modern Detergent Powders*. Herman de Groot Academic Publisher: Wassenaar, 1995.

[13] A. A. Dolinsky. High-temperature spray drying. *Drying Technology*, 19(5):785–806, May 2001. doi:10.1081/DRT-100103770.

[14] T. M. El-Sayed, D. A. Wallack, and C. J. King. Changes in particle morphology during drying of drops of carbohydrate solutions and food liquids. 1. Effect of composition and drying conditions. *Industrial Engineering and Chemical Research*, 29 (12):2346 – 2354, December 1990. doi:10.1021/ie00108a007.

[15] T. Elperin and B. Krasovitov. Evaporation of liquid droplets containing small solid particles. *International Journal of Heat and Mass Transfer*, 38(12):2259–2267, August 1995. doi:10.1016/0017-9310(94)00337-U.

[16] M. Farid. A new approach to modelling of single droplet drying. *Chemical Engineering Science*, 58(13):2985–2993, July 2003. doi:10.1016/S0009-2509(03)00161-1.

[17] G. Ferrari, G. Meerdink, and P. Walstra. Drying kinetics for a single droplet of skim-milk. *Journal of Food Engineering*, 10(3):215–230, 1989. doi:10.1016/0260-8774(89)90027-7.

[18] D. D. Frey and C. J. King. Experimental and theoretical investigation of foam-spray drying. 1. Mathematical model for the drying of foams in the constant-rate period. *Journal of Industrial and Engineering Chemisty Fundamentals*, 25(4):723 – 730, 1986. doi:10.1021/i100024a041.

[19] C. G. Greenwald and C. J. King. The effects of design and opetating conditions on particle morphology for spray-dried foods. *Journal of Food Process Engineering*, 4 (3):171–187, July 1981. doi:10.1111/j.1745-4530.1981.tb00254.x.

[20] C. G. Greenwald and C. J. King. The mechanism of particle expansion in spray drying of foods. *AIChE Symposium Series*, 78(218):101–110, 1982.

[21] C. S. Handscomb. *Simualting Droplet Drying and Particle Formation in Spray Towers*. Phd thesis, University of Cambridge, Department of Chemical Engineering, November 2008.

[22] C. S. Handscomb, M. Kraft, and A. E. Bayly. A new model for the drying of droplets containing suspended solids. *Chemical Engineering Science*, In Press, 2008. doi:10.1016/j.ces.2008.04.051.

[23] C. S. Handscomb, M. Kraft, and A. E. Bayly. A new model for the drying of droplets containing suspended solids after shell formation. *Chemical Engineering Science*, 64(2):228–246, January 2009. doi:10.1016/j.ces.2008.10.019.

[24] J. P. Hecht and C. J. King. Spray drying: Influence of developing drop morphology on drying rates and retention of volatile substances. 1. Single drop experiments. *Industrial and Engineering Chemical Research*, 39(6):1756–1765, June 2000. doi:10.1021/ie9904652.

[25] J. P. Hecht and C. J. King. Spray drying: Influence of developing drop morphology on drying rates and retention of volatile substances. 2. Modeling. *Industrial and Engineering Chemical Research*, 39(6):1766–1774, June 2000. doi:10.1021/ie990464+.

[26] T. N. Hunter, G. J. Jameson, and E. J. Wanless. Determinatino of contact angles of nanosized silica particles by multi-angle single-wavelength ellipsometry. *Australian Journal of Chemistry*, 60(9):651–655, September 2007. doi:10.1071/CH07133.

[27] D. H. Huntington. The influence of the spray drying process on product properties. *Drying Technology*, 22(6):1261–1287, December 2004. doi:10.1081/DRT-120038730.

[28] A. R. Imre. Binary liquids under absolute negative pressure. *Periodica Polytechnica Chemical Engineering*, 44(1):39–48, 2000.

[29] M. Kadja and G. Bergeles. Modelling of slurry droplet drying. *Applied Thermal Engineering*, 23(7):829–844, May 2003. doi:10.1016/S1359-4311(03)00014-0.

[30] R. B. Keey. *Drying Principles and Practice*. Pergamon Press, 2nd edition, 1975.

[31] S. Kentish, M. Davidson, H. Hassan, and C. Bloore. Milk skin formation during drying. *Chemical Engineering Science*, 60(3):635–646, February 2005. doi:10.1016/j.ces.2004.08.033.

[32] T. Langrish and D. Fletcher. Prospects for the modelling and design of spray dryers in the 21st century. *Drying Technology*, 21(2):197–215, January 2003. doi:10.1081/DRT-120017743.

[33] H. Maris and S. Balibar. Negative pressures and cavitation in liquid helium. *Physics Today*, 53(2):29–34, February 2000. doi:10.1063/1.882962.

[34] K. Masters. *Spray Drying Handbook*. Longman Scientific and Technical, UK, 5th edition, 1992.

[35] M. Mezhericher, A. Levy, and I. Borde. Theoretical drying model of single droplets containing insoluble or dissolved solids. *Drying Technology*, 25(6):1025–1032, June 2007. doi:10.1080/07373930701394902.

[36] H. Minoshima, K. Matsushima, H. Liang, and K. Shinohara. Basic model of spray drying granulation. *Journal of Chemical Engineering of Japan*, 34(4):472–478, 2001. doi:10.1252/jcej.34.472.

[37] H. Minoshima, K. Matsushima, H. Liang, and K. Shinohara. Estimation of diameter of granule prepared by spray drying of slurry with fast and easy evaporation. *Journal of Chemical Engineering of Japan*, 35(9):880–885, 2002. doi:10.1252/jcej.35.880.

[38] S. Nešić and J. Vodnik. Kinetics of droplet evaporation. *Chemical Engineering Science*, 46(2):527–537, 1991. doi:10.1016/0009-2509(91)80013-O.

[39] D. E. Oakley. Produce uniform particles by spray drying. *Chemical Engineering Progress*, 10(1):48–54, 1997.

[40] W. E. Ranz and W. R. Marshall. Evaporation from drops part I. *Chemical Engineering Progress*, 48(3):141–6, 1952.

[41] Y. Sano and R. B. Keey. The drying of a spherical partical containing colloidal material into a hollow sphere. *Chemical Engineering Science*, 37(6):881–889, 1982. doi:10.1016/0009-2509(82)80176-0.

[42] G. W. Scherer. Theory of drying. *Journal of the American Ceramic Society*, 73(1): 3–14, January 1990. doi:10.1111/j.1151-2916.1990.tb05082.x.

[43] G. W. Scherer. Bending of gel beams: method for characterizing elastic properties and permeability. *Journal of Non-Crystalline Solids*, 142:18–35, 1992. doi:10.1016/S0022-3093(05)80003-1.

[44] G. W. Scherer. Hydraulic radius and mesh size of gels. *Journal of Sol-Gel Science and Technology*, 1(3):285–291, January 1994. doi:10.1007/BF00486171.

[45] E. U. Schlünder. Drying of porous material during the constant and the falling rate period: A critical review of exisiting hypotheses. *Drying Technology*, 22(6):1517–1532, December 2004. doi:10.1081/DRT-120038738.

[46] P. Seydel, J. Blömer, and J. Bertling. Modeling particle formation at spray drying using population balances. *Drying Technology*, 24(2):137–146, March 2006. doi:10.1080/07373930600558912.

[47] D. M. Smith, G. W. Scherer, and J. M. Anderson. Shrinkage during drying of silica gel. *Journal of Non-Crystalline Solids*, 188(3):191–206, October 1995. doi:10.1016/0022-3093(95)00187-5.

[48] D. B. Spalding. *Convective Mass Transfer*. Edward Arnold, 1st edition, 1963.

[49] N. R. Tas, P. Mela, T. Kramer, J. W. Berenschot, and A. Van den Berg. Water plugs in nanochannels under negative pressure. In *Proceedings of the 7th International Conference on Miniaturized Chemical and Biochemical Analysis Systems*, pages 13–16, October 2003.

[50] S. P. Timoshenko. *Theory of Elastic Stability*. McGraw-Hill, 1st edition, 1936.

[51] N. Tsapis, E. Dufresne, S. Sinha, C. Riera, J. Hutchinson, L. Mahadevan, and D. Weitz. Onset of buckling in drying droplets of colloidal suspensions. *Physical Review Letters*, 94(1):018302, January 2005. doi:10.1103/PhysRevLett.94.018302.

[52] J. Van der Lijn. *Simulation of Heat and Mass Transfer in Spray Drying*. PhD thesis, University of Wageningen, 1976.

[53] J. G. P. Verhey. Vacuole formation in spray powder particles 1. air incorporation and bubble expansion. *Netherlands Milk and Dairy Journal*, 26:186–202, 1972.

[54] D. Walton and C. Mumford. The morphology of spray-dried particles - the effect of process variables upon the morphology of spray-dried particles. *Chemical Engineering Research and Design*, 77:442–460, July 1999. doi:10.1205/026387699526296.

[55] D. Walton and C. Mumford. Spray dried products - characterization of particle morphology. *Chemical Engineering Research and Design*, 77:21–37, January 1999. doi:10.1205/026387699525846.

[56] S. R. L. Werner, R. L. Edmonds, J. R. Jones, J. E. Bronlund, and A. H. J. Paterson. Single droplet drying: Transition from the effective diffusion model to a modified receding interface model. *Powder Technology*, 179(3):184–189, January 2008. doi:10.1016/j.powtec.2007.06.009.

[57] S. R. L. Werner, R. L. Edmonds, J. R. Jones, and A. H. J. Paterson. Single droplet drying. 2. maltodextrin DE5 drying kinetics and mathematical model validation. Submitted for publication, 2008.

[58] S. R. L. Werner, R. L. Edmonds, A. H. J. Paterson, J. E. Bronllund, and J. R. Jones. Single droplet drying. 1. review of major model types, controlling mechanisms and the constant internal temperature assumption. Submitted for publication, 2008.

[59] S. Whitaker. Simultaneous heat, mass, and momentum transfer in porous media: a theory of drying. *Advances in Heat Transfer*, 13:119–203, 1977.

[60] A. E. Wijlhuizen, P. J. A. M. Kerkhof, and S. Bruin. Theoretical study of the inactivation of phosphatase during spray drying of skim-milk. *Chemical Engineering Science*, 34(5):651–660, 1979. doi:10.1016/0009-2509(79)85110-6.